Investigation of Magnetic Field Signals During Vortex-Induced Pressure Drops at InSight

List of Authors:
Shea N. Thorne[1], Catherine L. Johnson[1,2], Anna Mittelholz[3], Benoit Langlais[4], Ralph Lorenz[5], Naomi Murdoch[6], Aymeric Spiga[7,8], Suzanne E. Smrekar[9], W. Bruce Banerdt[9]

Affiliations:
[1]Department of Earth, Ocean and Atmospheric Sciences, The University of British Columbia, Vancouver, Canada.
[2]Planetary Science Institute, Tucson, Arizona, USA.
[3]Department of Earth and Planetary Sciences, Harvard University, Cambridge, MA, USA.
[4] Laboratoire de Planétologie et Géosciences, UMR 6112, Nantes Université, Université d'Angers, Le Mans Université, CNRS, Nantes, France.
[5]Johns Hopkins Applied Physics Laboratory, Laurel, MD, USA.
[6]ISAE-SUPAERO, Université de Toulouse, Toulouse, France.
[7] Laboratoire de Météorologie Dynamique/Institut Pierre-Simon Laplace, Sorbonne Université, Centre National de la Recherche Scientifique, École Polytechnique, École Normale´ Supérieure, Campus Pierre et Marie Curie BC99, Paris, France.
[8]Institut Universitaire de France, Paris, France.
[9]Jet Propulsion Laboratory, California Institute of Technology, Pasadena, CA, USA

Corresponding author: Shea Thorne (sthorne@eoas.ubc.ca, 302 Earth and Oceans Science 6339 Stores Road V6T 1Z4 Vancouver, BC, Canada)

Abstract
The NASA InSight lander has recorded many pressure drops attributed to convective vortices during its first full year of data collection. However, although dust-carrying vortices (dust devils) are a common phenomenon on Mars, they have not been observed in InSight images. On Earth, magnetic signals associated with some dust devils have been reported. Data from the InSight Fluxgate Magnetometer (IFG) provide the first opportunity for similar investigations on Mars. Here, we evaluate whether magnetic signals are associated with daytime vortices. We incorporate observations of environmental conditions, measurements of ground tilt from seismic data, and data from the lander's solar panels, and consider the potential for dust-laden vortices to generate observable magnetic field signals. We find that 7.7% of pressure drop events greater than 1 Pa show a resolvable magnetic field signal at the time of the pressure drops. The resolvable magnetic signals, typically seen on the horizontal field components, are less than 1 nT in amplitude, and have no clear correlation with local time, duration, or pressure drop magnitude. During nine pressure drop events we found smoothly varying magnetic signals of at least 0.3 nT on any one component. To investigate the origin of these magnetic signals we evaluated three possible sources: solar array currents, ground and lander tilt, and triboelectric effects of lofted dust. We find that SAC and tilt could contribute a change in the magnetic field but cannot solely explain the observed signals. The observed changes in field strength could theoretically be produced via triboelectric effects, but only in the case of exceptionally large dust devils that pass close to the lander. The lack of imaged dust devils and the small number of observed magnetic signatures despite numerous measured pressure drops is consistent with at most a small

proportion of dust laden convective vortices at InSight and associated predicted triboelectric effects.

Keywords: Dust devils, Convective vortices, Magnetic Fields, Mars, InSight, Triboelectricity

1 Introduction

The Interior Exploration using Seismic Investigations, Geodesy and Heat Transport (InSight) Mars Lander touched down on November 26, 2018 in Elysium Planitia. It carries the Auxiliary Payload Sensor Suite (APSS) that includes the InSight FluxGate magnetometer (IFG). The IFG is the first magnetometer on the surface of Mars, and thus provides a unique opportunity to study the static crustal and time-varying external magnetic fields below the martian ionosphere (Banfield et al., 2018). To date, the crustal magnetic field strength, ~2000 nT, and direction as well as diurnal magnetic field variations measured by the IFG have been investigated (Banerdt et al., 2020; Johnson et al., 2020; Mittelholz et al., 2020). However, the IFG has also measured aperiodic magnetic signals that occur over timescales of seconds to minutes. Here we use IFG data, together with observations of environmental conditions around the lander by APSS (Banfield et al., 2018), measurements of ground tilt from seismic data, and data from the InSight's solar panels, to evaluate whether magnetic signals are associated with daytime convective vortices. Of specific interest is whether potentially dust-laden convective vortices, i.e., dust devils, generate observable magnetic field signals at the InSight landing site.

Dust devils (DDs) were first observed on Mars in Viking Orbiter images and have been subsequently imaged by many missions, either via direct imaging or by the tracks left from the passage of DDs (Balme & Greeley, 2006; Thomas & Gierasch, 1985). Martian DDs provide an important mechanism for dust injection into the atmosphere (Kahre, Murphy, & Haberle, 2006) as well as for the vertical transport of heat (Renno et al. 2004), and have been proposed to maintain current flow among atmospheric regions (Harrison et al., 2016). DDs also contribute to global atmospheric conditions via their effects on convective circulation and a multi-year study of martian DD heights found that they correlate seasonally with the thickness of the planetary boundary layer, a descriptive measure of the vigor of convective atmospheric activity (Fenton & Lorenz, 2015). The electrification of DDs could also affect martian habitability as they have been purported to induce production of H_2O_2 which could be responsible for scavenging organic material or reducing the residence time of methane gas in the martian atmosphere (Atreya et al., 2006). Although that process has been shown to have limited impact (Kok & Renno, 2009), the electric and magnetic signatures of dusty atmospheric structures need to be better assessed. DDs are specifically important to planetary missions because of the possibility for dust deposition on, or removal from, solar panels that in turn can shorten or extend mission operations, respectively (Lorenz & Reiss, 2015), and their electromagnetic noise has been hypothesized to affect communication equipment (Harrison et al., 2016).

October 2020 marked a full martian year of data collection by the pressure sensor instrument on InSight, providing a set of 11,251 pressure drops which were recently compiled (Spiga et al., 2021; Chatain, Spiga, et. al. 2021). The InSight landing site is the most active site for vortices of all landed martian missions to date (Banerdt et al., 2020). Convective vortices are classified as DDs if they loft dust, but the fraction of DDs to dustless vortices is not well understood (Lorenz & Jackson, 2015; Spiga et al., 2016). To date InSight has not imaged any DDs despite targeted surveys (Banfield et al., 2020; Lorenz, Spiga, et al., 2021) but DD tracks around the lander have

been observed via satellite imagery (Perrin et al., 2020) and by InSight's cameras (Charalambous et al., 2021). A recent study of parameters inferred for a subset of these vortices together with advective wind speeds suggests that high wind speeds at the InSight landing site may suppress the formation of DDs (Jackson et al., 2021).

The uplift of a passing vortex is known to also affect seismic measurements (Lorenz et al., 2015). InSight's Seismic Experiment for Interior Structure (SEIS) instrument and the pressure sensor have observed simultaneous seismic and pressure signals due to convective vortices (Lognonné et al., 2020, Murdoch et al., 2021). One such observation also corresponds to a newly-formed DD track that came within 19 m of the lander, and the track was imaged from the lander's camera and from orbit (Banerdt et al., 2020). These joint observations permitted estimates of the vortex properties (e.g., diameter), as well as the elastic rigidity (compliance) of the ground near the landing site.

On Earth, there have been two observations of magnetic signals from dust carrying vortices in the form of ultra-low frequency electromagnetic emission in conjunction with the passage of a DD, at distances up to 100's of meters from the electromagnetic sensors (Farrell et al., 2004; Houser, Farrell, & Metzger, 2003). The first such DD, reported by Houser et al. (2003) was approximately 10 meters wide and 200 meters tall with continuous broadband electromagnetic emission at frequencies below 50 Hz with peaks near 10 Hz, while the second reported by Farrell et al., 2004 again detected magnetic emission between 1-10 Hz (see further Figures 3 and 4 in Farrell et al., 2004), reporting a magnetic field of ~ 0.1 nT immediately outside the DD. One possible origin for the magnetic field signals, discussed in the terrestrial literature is cyclostrophic motion of triboelectrically charged lofted dust, behaving as a magnetic solenoid (Farrell et al., 2006; Kurgansky, Baez, & Ovalle, 2007).

In this study we look for possible DD signatures in the magnetic field measurements recorded by InSight. Assuming they can be tied to other meteorological information, they could help constrain the subset of the convective vortices that are DDs (Houser et al., 2003). A few pressure drop events have been found to exhibit magnetic signals; however the origin of these was unclear (Charalambous et al., 2021; Johnson et al., 2020). A passing vortex, if a DD, could be observed in IFG data via one or more of the following possible mechanisms: (1) Triboelectrically charged lofted dust, as suggested for terrestrial DD magnetic emission (Farrell et al., 2006; Kurgansky, Baez, & Ovalle, 2007), (2) Changing solar array currents as a result of entrained dust of a passing DD obscuring the solar arrays (as observed at InSight during transits of Phobos (Stähler et al., 2020), (3) Ground tilting resulting from the pressure lows at the center of convective vortices (Lognonné et al., 2020, Murdoch et al., 2021) that changes the orientation of the IFG in the ambient crustal magnetic field, and (4) similarly, wind-induced tilt of the lander as explored previously for the seismometer on the lander deck (Murdoch et al, 2017, Panning et al., 2020). The goal is therefore to establish, if, when, and why pressure drops at the InSight lander have associated magnetic signals and in particular to evaluate whether any such signals can be attributed to DDs. Here, we first identify the fraction of pressure drop events that have a resolvable magnetic signature. These resolvable events and their characteristics are then used to evaluate the four mechanisms through which a vortex or DD could create a magnetic signal.

2 Resolvable Magnetic Signatures at the Times of Pressure Drops

2.1 IFG Data during pressure drops

From the set of 11,251 pressure drops over the first martian year of InSight data collection (Spiga et al., 2021; Chatain, Spiga, et. al. 2021), we selected the 1061 events that exhibit pressure drops of at least 1 Pa (Figure 1). This excludes small events unlikely to loft dust (Lorenz, Spiga, et al., 2021).

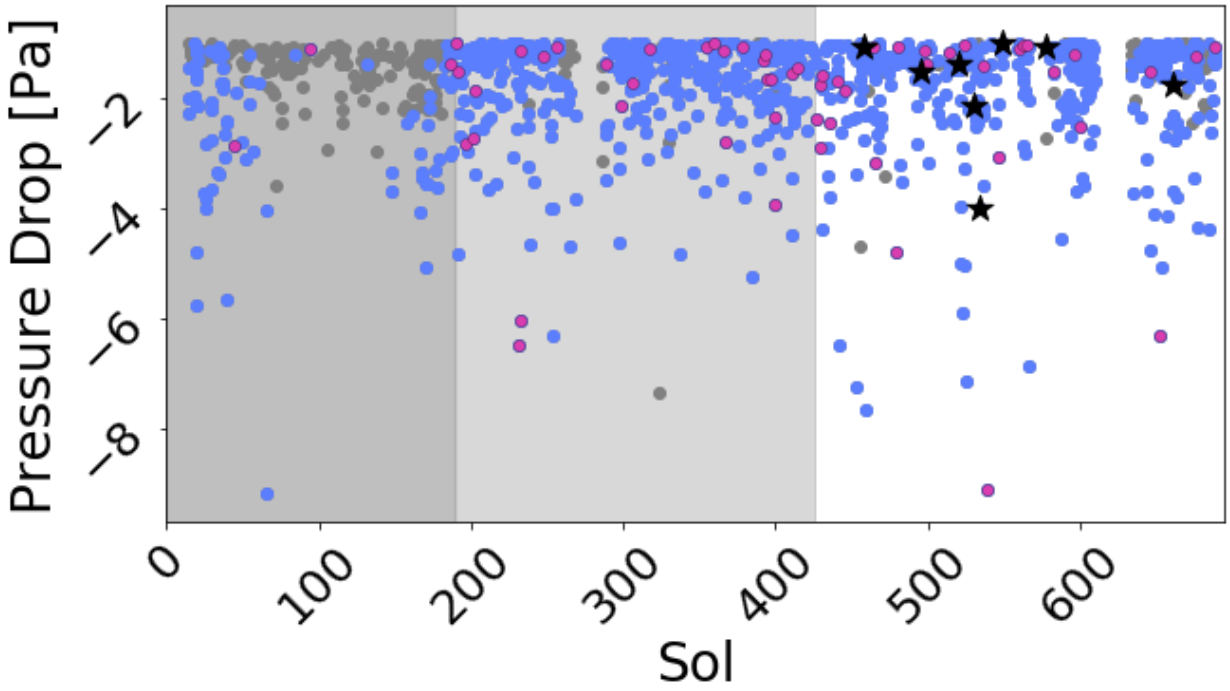


Figure 1*. 1061 pressure drops greater than 1 Pa recorded by InSight during the first full Martian year of observations. At sol 189 the IFG sampling rate for continuous data increased from 0.2 Hz to 2 Hz (dark gray to light gray background transition) and at sol 426 the solar array current data cadence increased from 0.0167 Hz to 0.25 Hz when recorded (light gray background to white background). All events (gray), events with either continuous 2 Hz IFG data or 20 Hz data down-sampled to 2 Hz (blue, N = 862), events with a standard deviation signal to noise ratio (SNR_σ) >= 2 (pink, N= 66), and the subset (N =8) of SNR_σ >= 2 events with 0.25 Hz solar array current data (black stars).*

The continuous sampling rate of the IFG was initially 0.2 Hz, and on sol 189 it was increased to 2 Hz. For short timeframes of interest 20 Hz data can be requested and these are available for some of the observed pressure drop times. Intermittent outages of the data acquisition electronics for IFG (the Payload Auxiliary Electronics (PAE)) resulted in data gaps in the IFG and other meteorological sensor data sets. For one 10-day interval, sols 261 – 269, the continuous sampling rate was decreased again to 0.2 Hz because of downlink limitations just before solar conjunction and a spacecraft anomaly (sols 270 – 283) led to a subsequent data gap until communication with the spacecraft could be resumed. Further PAE anomalies occurred but were mostly addressed within a time frame of a few hours.

We initially used 0.2 Hz data (recorded or decimated from higher frequency data) to assess the overall shape and structure of magnetic signals at the times of the pressure drops (e.g., Figure 2), but found they lacked sufficient temporal resolution to characterize the magnetic field in detail during pressure drops. Therefore, we retained 879 events for which either 2 Hz or 20 Hz data (V6; Joy et al., 2019) were available, and the 20 Hz data were down-sampled to 2 Hz to create a consistent data set, using the same approach applied to the IFG data set (Joy et al., 2019). We inspected these 879 events by hand to identify any magnetic signals of artificial origin, i.e., lander activities, at the times of pressure drops. Such activities include the lander wake on/off commands, communications, or movement of the lander's robotic arm, all of which generate magnetic signals that are not completely removed from the calibrated IFG data (Johnson et al., 2020; Mittelholz et al., 2020; Thorne et al., 2020). 17 events had magnetic field signals with clear artificial origins and were discarded, resulting in a final set of 862 events. Magnetic field components are reported in the InSight lander level coordinate system in which X points north, Y points east and Z points down (Johnson et al., 2020; Joy et al., 2019).

2.2 Event Identification and Resulting Statistics

Mars exhibits diurnal magnetic field changes as well as shorter period variations throughout a sol (Mittelholz et al., 2020). As an example, we show the magnetic field for sols 529 – 539 (Figure 2); on one of these sols (534) a pressure drop with a resolvable magnetic field signal is seen (Figure 2C, discussed more below). As discussed in Mittelholz et al. (2020), the diurnal cycle (Figure 2A) has a peak in the early to mid-morning. This is attributable, at least in part, to wind-driven ionospheric currents that in turn depend on atmospheric properties such as horizontal wind speed and electron density (see review in Mittelholz et al., 2020). Increased noise in the data is clearly seen on all sols between ~11:00 – 16:00 hrs, and this is inferred to result from short time-scale variability in solar array currents (Johnson et al., 2020). Although the example event occurs during a comparably "quiet" time (Figure 2A,B), during the event time frame (Figure 2C) the background noise is substantial, requiring care in identifying any magnetic signature of pressure drop events.

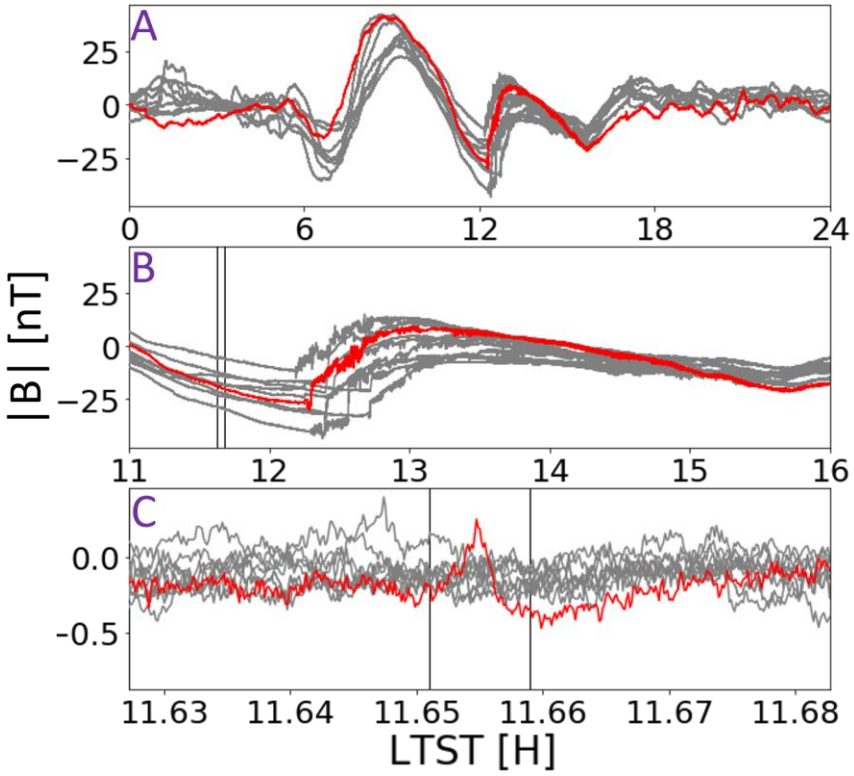


Figure 2. *IFG magnitude |B|, detrended over a full sol, plotted for 10 sols (529-539) with sol 534 (red), on which a convective vortex studied here occurs. (a) |B| over a full sol. (b) LTST ~11:00-16:00 with the time of event on sol 534 plotted in Figure 4A identified by vertical lines. (c) |B| during the corresponding LTST for which an event was detected on sol 534 (shown in Figure 4A), detrended over the time window shown to highlight the noise. Vertical lines show the duration of the event (28.8 seconds).*

We first assessed the typical variability in the field over the characteristic timescale of pressure drops at all local times (Figure 3). We compared this with the local magnetic field variability immediately before and after each of the 862 events, as well as with the variability during a pressure drop to assess whether magnetic signatures during the times of pressure drops can be distinguished from background fluctuations.

Pressure drop durations (twice the full-width-at-half-max, FWHM) were obtained via gaussian fitting of a 200 second interval of detrended pressure data centered on the pressure drop peak, following the methodology described in Murdoch et al. (2021). To capture the typical background variability in the field on the time scale of pressure drops, each sol with 2 Hz data first had a 60s running mean removed and was then divided into sections the length of the average duration of pressure drop events (21.7 seconds). The standard deviation (σ) in each field component for each section was computed, binned into half hour local time bins, and the median value of σ in each bin was computed (Figure 3). For pressure drop events, the local background variability in each magnetic field component was quantified by the average σ of the magnetic field in windows 1.5 times the duration of the individual event, directly before and after the

pressure drop (σ^{bk}) (the dark grey shading in Figure 4). The magnetic field variability during each event was characterized by the σ during the pressure drop (σ^{pd}) (the light grey shading in Figure 4).

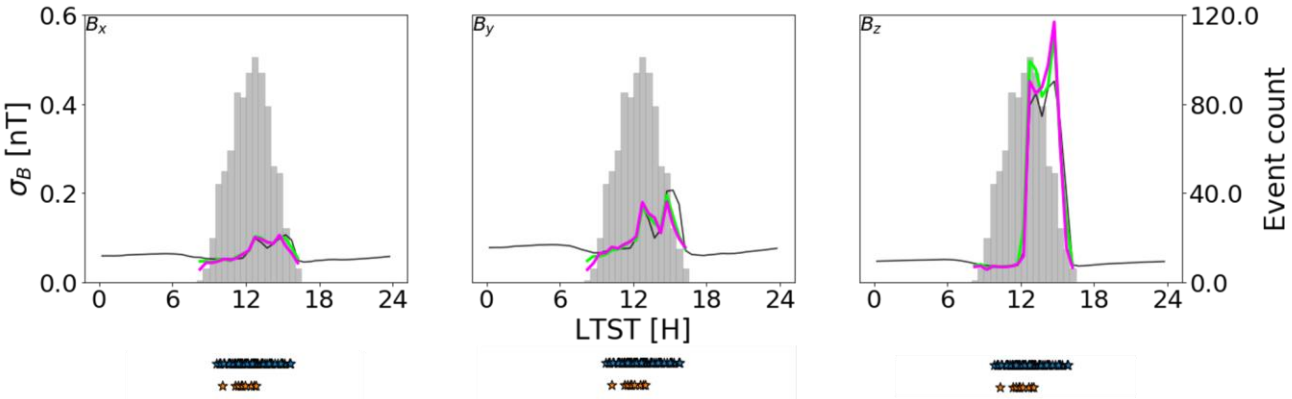


Figure 3. *Median standard deviation in each magnetic field component, σ, during (pink) and directly surrounding (green) pressure drop events, as well as the ambient variability in the field over the characteristic time scale of a pressure drop (black), all shown for the first year of the mission and binned in 30 min local true solar time (LTST) bins. The number of pressure drop events per bin is shown by gray bars. Blue stars are plotted below the x-axis at the local time for each of the 66 events with a $SNR_\sigma >= 2$ in at least one magnetic field component. Orange stars show the 9 events highlighted in section 2.3.*

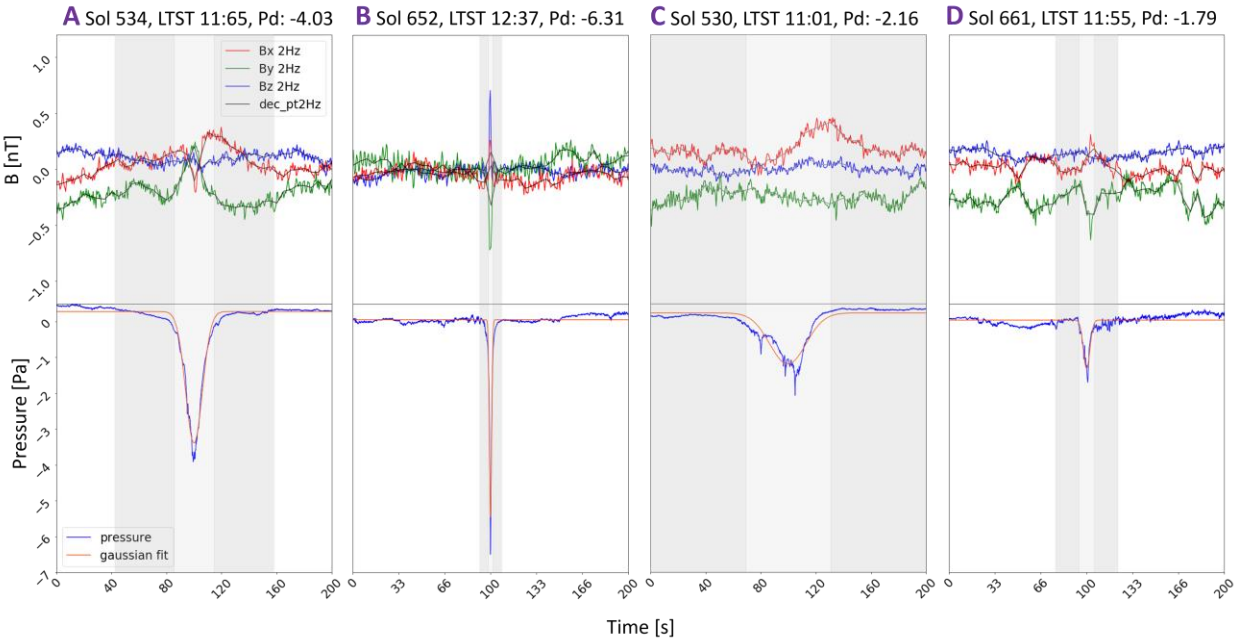


Figure 4*. A-D show 4 examples of pressure drop events with sol number, local time of pressure drop peak, and pressure drop (Pd) in Pa identified by Spiga et al., 2021. Top row: North (B_X - Red), East (B_Y - Green) and Vertical Down (B_Z - Blue) magnetic field components during each pressure drop (light grey shading) and the surrounding background period (darker grey shading,*

1.5 times the event duration before and after the event). 2 Hz (colors) and decimated 0.2 Hz (blackline) data after subtraction of a 60s moving average are shown. Bottom row: pressure drop (blue) with gaussian fit (red). A and D have $SNR_\sigma > 2$ *and* $SNR_{P2P} > 1.8$ *in the* B_Y component, B has SNR_σ *and* SNR_{P2P} *above their respective thresholds in all 3 components, and* C has SNR_σ*>2 in* B_Y.

Overall, the variability in the ambient magnetic field increases substantially between noon and 4pm local true solar time on each sol (Figures 2,3). This is in part related to varying current draws from the solar array panels and other lander activities (Johnson et al., 2020; Mittelholz et al., 2020; Lorenz et al., 2020). The σ immediately before and after an event, as well as during an event, are similar in amplitude to the typical variability in the field. This suggests that, on average, magnetic signals at times of pressure drops are not significantly different from those in the immediate surrounding intervals or the typical background variability at that local time. Furthermore, the typical variability in the vertical magnetic field component is much larger than on the horizontal channels, typical ~0.5 nT between noon and 4pm LTST. This analysis also shows that identification of signals in the IFG data is not trivial due to typical short-term variability in the data.

As we had no a priori expectations as to how a DD might manifest in the IFG data, we used two methods to quantify the signals during individual events. We first determined the signal to noise ratio (SNR) for each of the 862 events to systematically identify those with a resolvable magnetic signature. The signal for each event, as identified in the pressure data, was detrended with a 60 second running mean (described above), to remove longer time scale variations unassociated with the pressure drop. We defined the standard deviation signal to noise ratio SNR_σ as the ratio $\sigma^{pd} / \sigma^{bk}$. We found that 66 of the 862 events recorded at 2 Hz had a SNR_σ greater than or equal to 2 on at least one magnetic field component (Figure 1).

We also implemented a selection scheme in which we replaced σ^{pd} and σ^{bk} with the maximum excursion (i.e., the range or peak-to-peak amplitude) during and before/after the event respectively and recomputed the SNR using these values, termed the SNR_{P2P}. We found that this method systematically resulted in the detection of fewer high SNR events c.f. the standard deviation approach. To compare whether the two approaches identified similar populations of events we first plotted empirical cumulative distribution functions for SNR_{P2P} and SNR_σ (for each component). We used these to determine the SNR_{P2P} value that corresponds to the same number of events with resolvable magnetic field signals as identified using a $SNR_\sigma = 2$. This resulted in a $SNR_{P2P} = 1.8$. We found that 46 of the 66 events (70%) identified using the $SNR_\sigma = 2$ were also identified using $SNR_{P2P} = 1.8$ indicating substantial, but not complete, overlap in the populations (see details in Supplementary Table 1 and Catalogue). Although the SNR_{P2P} might seem a more obvious approach, noise in the IFG data can result in spurious range measurements and is more sensitive to outliers. We thus chose to use the events identified using SNR_σ for further analyses. Examples for three events are shown in Figure 4, and all events identified with either the standard deviation or range approach are catalogued in the Supplemental Information.

The 66 high SNR_σ events correspond to 6.2% of all pressure drops > 1 Pa and 7.7% of the 862 events with IFG data. In detail, we find that for most events only one magnetic field component has a $SNR_\sigma >= 2$. For B_X, B_Y, and B_Z this occurred for 3.0% (N=26), 4.1% (N=35), and 2.7%

(N=23) of the 862 pressure drops respectively (Figure 5). We further observe that resolvable events have no clear correlation with local time, duration, and pressure drop magnitude (Figure 6). The local times of all 66 SNR_σ events (shown with blue stars in Figure 3) are seen to have a similar local time distribution to that of the pressure drop events overall.

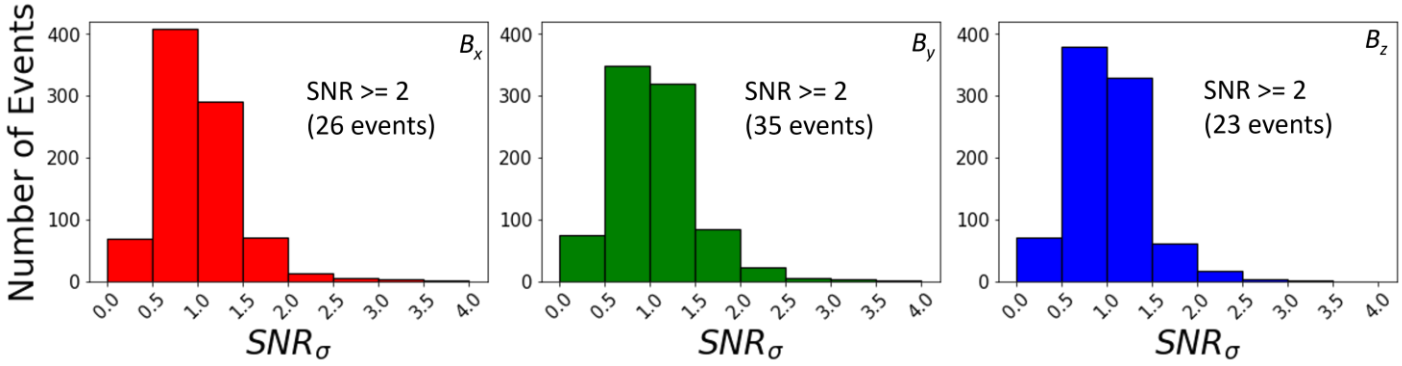


Figure 5. *Histograms of the standard deviation signal-to-noise ratios (SNR_σ) for the north (B_X), east (B_Y) and vertical down (B_Z) magnetic field components. The numbers of events with* SNR_σ *>=2 are given. Seven events with* SNR_σ *>4 are not shown (2 in B_X, 2 in B_Y and 3 in B_Z).*

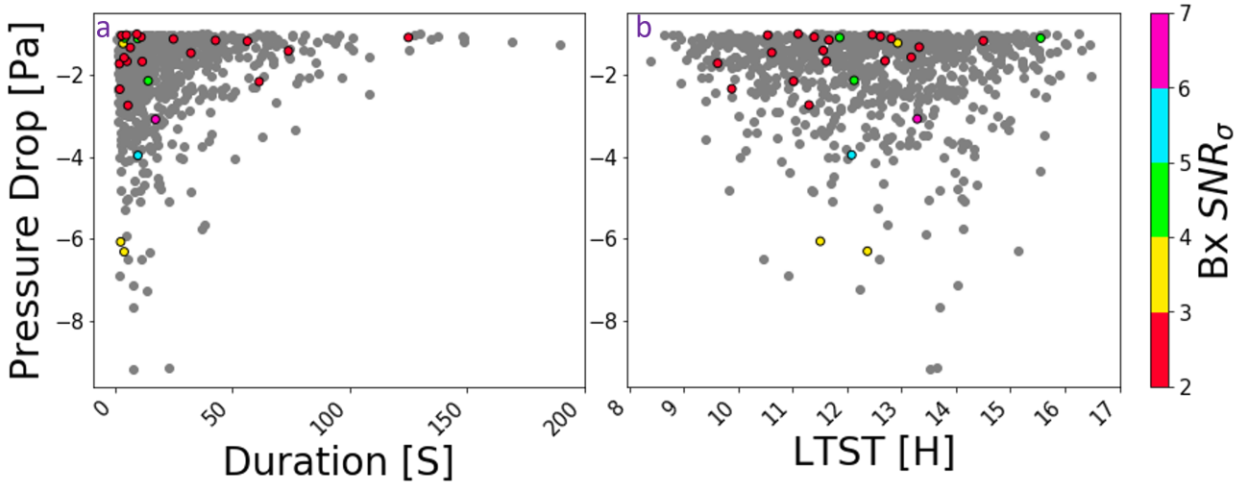


Figure 6. *Pressure drop magnitude for events with SNR_σ >= 2 in the B_X magnetic field component (colored dots), compared with the overall population of pressure drops greater than 1 Pa examined here. Pressure drop versus (a) event duration (2 x FWHM), and (b) local true solar time (LTST). The results for events with SNR_σ >= 2 in B_Y and B_Z are similar.*

We evaluated whether this occurrence rate of high SNR_σ events occurs randomly in the IFG data set as follows. For every sol over the martian year with 2 Hz IFG, we computed a SNR for local time sections of the sol with the length of the average duration of pressure drop events, by dividing the σ during the short section by the average σ of the sections before and after it. We found that for B_X, B_Y, and B_Z, a SNR_σ >= 2 occurred for 2.5%, 2.0%, and 2.3% of the 469808 segments, less than the occurrence rate of a SNR_σ >= 2 during the times of pressure drops. This analysis confirms that our identification of events is statistically significant, and we reject the hypothesis that our identifications are not associated with any events.

2.3 Magnetic Field Signals During Pressure Drops

Our event detection method identified 66 pressure drop events, 8 of which have concurrent solar array current data (see Supplementary Figure 1 and Section 3.1). These events are reported together with figures and their statistics in the supplementary information catalog which also includes the events identified only by the SNR_{P2P} method and all events with pressure drop magnitudes >= 3.8 Pa (123 events total as listed in Supplementary Table 1). The set of resolvable events (as identified by both selection methods) and large pressure events was visually examined for magnetic signals that varied smoothly during the pressure drop duration while also showing a clear peak-to-peak signal of at least 0.3 nT on any one component. We found that only 9 events matched these criteria. Three such events are displayed in Figure 4 (A, B, & D) and the remaining 6 are shown in Figure 7. For these events, the components that show the smoothly varying signals > 0.3 nT during the pressure drop are observed mostly B_X and B_Y (consistent with the lower noise level on these channels) and have an average peak-to-peak signal of 0.8 nT with a maximum observed range of 2.7 nT (B_Y in Figure 7F).

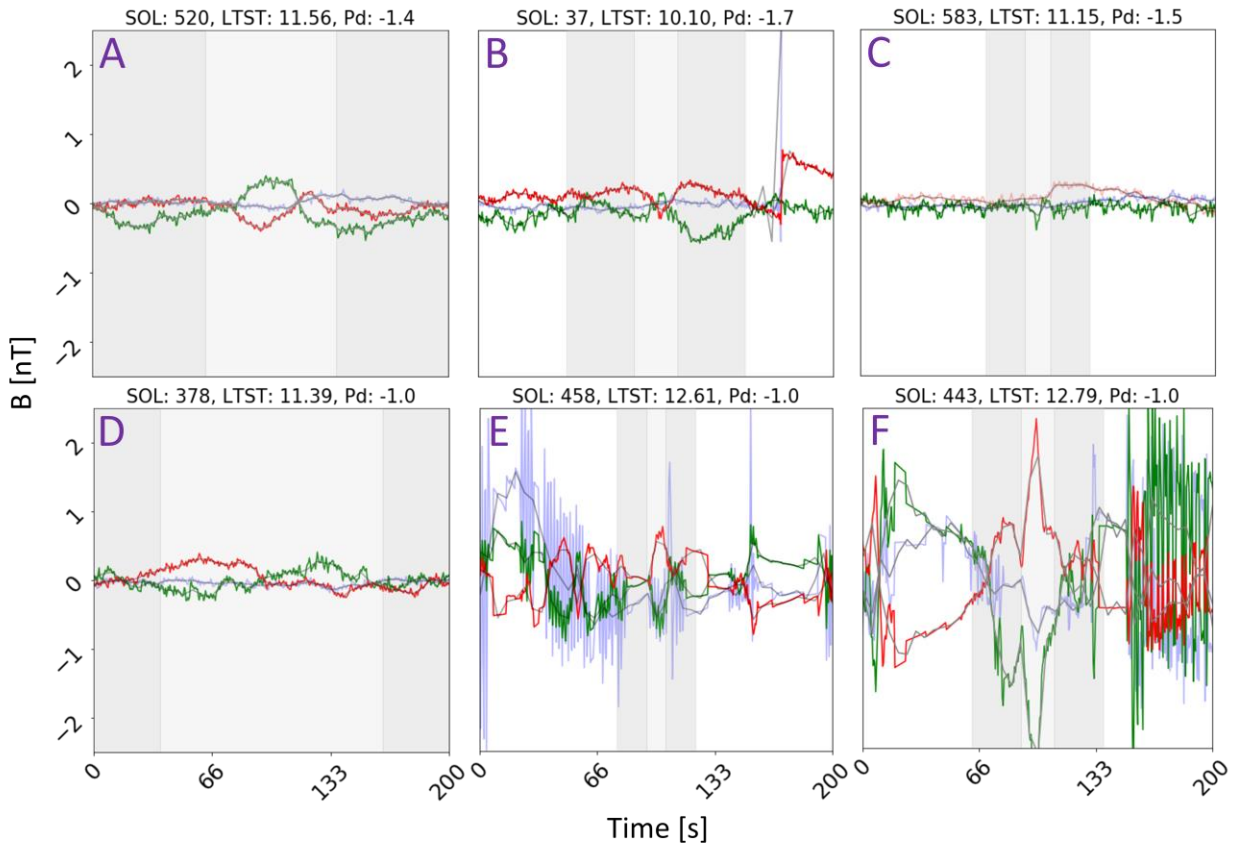


Figure 7*. A-F show B_X (red), B_Y (green) and B_Z (blue) for 6 resolvable events with smoothly varying magnetic signals during the pressure drop in one or more component featuring a peak-to-peak signal > .3 nT, plotted in the same style as top row of Figure 4. To highlight the identified signals, components that did not fit our selection criteria have increased transparency. The panels are titled with sol number, local time of pressure drop peak, and pressure drop (Pd) in Pa as identified by Spiga et al., 2021.*

We consider these 9 events the best candidate examples of magnetic field signals during pressure drops of the 862 events examined. Figures 7E and 7F show the challenges associated with identifying signals in noisy IFG data. Although the remaining events with high SNR may contain resolvable signals, the signals are either < ~0.1 nT or they occur during times of noisy magnetic field measurements as illustrated by Figure 2. As shown in Figure 3, the 9 events cluster in local time in the early part of the day and before the onset of the typical increase in variability in the ambient magnetic field. This is in contrast to the local times of all 66 SNR_σ events which have a similar local time distribution to that of all pressure drop events.

3 Discussion

We investigate three possible sources of the resolvable magnetic signals during the times of pressure drops: solar array currents, ground and lander tilt, and triboelectric effects. We then synthesize these results drawing on other InSight observations related to dust movement and DD.

3.1 Solar Array Currents

We investigated whether there is a correlation between changes in the solar array currents and magnetic signals to assess the possibility that a change in current caused by a DD leads to a change in the magnetic field. This could occur if lofted dust carried by DDs directly reduces solar incidence on the panels and thus leads to a drop in the current. Alternatively, increases in the solar array currents are possible as dust within a DD can scatter sunlight onto the arrays (Lorenz & Jackson, 2015). The effect could occur on either or both solar panels, depending on the relative orientations of the passing DD, the sun, and the solar panels. The change in solar array currents could have an attendant signal in the magnetic field measured by the IFG that together could help discern dust-free vortices from DDs. Drops in solar flux due to obscuration of solar cells by DDs have been observed on Earth (Lorenz & Jackson, 2015). At InSight, magnetic signals have been observed at the times of drops in the currents generated by the solar arrays during the Phobos and Deimos transits and the associated temporary darkening (Stähler et al., 2020).

The relevant solar array current (SAC) data for determining insolation are reported via 2 channels, 771 and 791. They indicate insolation on the east and west solar arrays respectively, the magnitude of which is relayed through currents from each solar array (Lorenz et al., 2020). Solar array currents were recorded at a sampling interval of ~30 seconds until Sol 426, when the sampling rate was increased to 4 seconds. However, InSight SAC data are only recorded when the lander is awake, i.e., not continuously (Lorenz et al., 2020) and long gaps in data coverage on any individual sol are present (see Figure 4 in Mittelholz et al., 2020). Because of the intermittent SAC data, a model of daily solar array currents generated to fit data gaps is fit to the data points as discussed in Joy et al. (2019), and interpolated to the cadence of the IFG data to correct IFG data for solar array currents. As a result, low frequency variations in the currents drawn by InSight's solar arrays are generally accounted for in the processing of magnetometer data, but variations on the time scales of pressure drops are not modeled and could contribute to IFG signals (Joy et al., 2019; Mittelholz et al., 2020).

To investigate whether the magnetic field at the time of a pressure drop is correlated with solar array current signals, we required SAC data throughout the pressure drop and corresponding flanking periods at a high enough cadence to resolve a change in current during the drop. We

thus examined pressure drop events with durations greater than or equal to 8 seconds for which 0.25 Hz SAC data were available (i.e., on or after Sol 426), resulting in 73 events (see Figure 1). This threshold for the pressure drop duration excludes the two DD events identified in the Lorenz, Lemmon, & Maki, (2021) SAC survey.

Of the 73 pressure drop events that fit the SAC data criteria, only eight of them have magnetic field components with a SNR_{σ} >= 2 and three of the eight also have a SNR_{P2P} that exceeds the SNR_{P2P} = 1.8 detection threshold (including Supplementary Figure 1C). Of the eight events, the magnetic signal is typically observed on only one of the X, Y, or Z IFG components, and not consistently on a specific component (the first 8 events listed in Supplementary Table 1). IFG signals are observed to be present both with and without concurrent SAC changes (Supplementary Figure 1). Additionally, pressure drops with low IFG SNR_{σ} (unresolvable) are commonly observed with and without SAC dips. We conclude that the SACs cannot be the only source of magnetic field signal during pressure drop events.

3.2 Ground or Lander Tilt

3.2.1 Ground Tilt

Tilting of the InSight lander by ground motion could also be responsible for a change in magnetic signal. As a DD or convective vortex is characterized by lower pressure in its center, its passage can be observed as the negative load deforms the surface, generating ground tilt (Banerdt et al., 2020; Murdoch et al., 2021).

The magnetic signal from a tilt of the lander due to ground motion caused by the low-pressure field of a convective vortex can be approximated as a small rotation **(**α**)** in the magnetometer orientation about a horizontal axis in the lander's reference frame. This results in a change in the orientation of the IFG with respect to the background crustal magnetic field, producing a change in the individual components, but leaving the magnitude of the overall signal unchanged, i.e. the new field $\boldsymbol{B}' = \boldsymbol{B} + \Delta\boldsymbol{B}$, where $|\boldsymbol{B}'| = |\boldsymbol{B}|$ Some geometry and algebra yield an expression for $\Delta B = |\Delta\boldsymbol{B}|$

$$\Delta B = B\, 4 \sin\left(\frac{\alpha}{4}\right) \cos\left(\frac{\alpha}{4}\right)$$

We calculate values for ΔB for ground tilts up to 10^{-2} degrees assuming a surface field strength B of 2000 nT at InSight (Johnson et al., 2020; Figure 8). Lorenz et al. (2015) reported terrestrial observations of ground tilts of ~10^{-7} ° correlated with long period (>9 second) convective vortices identified by pressure drops. This terrestrial value, if applicable at Mars, would result in a ΔB of 0.0002 nT, too small to be resolvable by the IFG. At InSight, seismic observations concurrent with pressure drops have been made because the seismometer is able to measure the resulting ground deformation (Banerdt et al., 2020; Lognonné et al., 2020; Murdoch et al., 2021). Stott et al. (2021) investigated ground tilt during the initial phase of the mission when the seismometer was still on the lander deck. They reported a maximum peak-to-peak tilt of ~0.002° on a three-months timescale, an estimate which captures motion of the regolith and thermoelastic tilting of the lander, both expected to be much larger effects than ground tilts during vortex events. This is supported by maximum ground tilt magnitudes between 10^{-9} ° and 10^{-6} ° for 492 vortex events (Figure 8 of Murdoch et al., 2021), all of which would have generated magnetic

signals too small to be resolvable by the IFG (Figure 8). The ground tilt required to cause a measured magnetic signal of 1 nT is ~0.03°, much larger than the expected or measured ground tilt values, and we therefore exclude this mechanism as the cause for magnetic signatures during pressure drops.

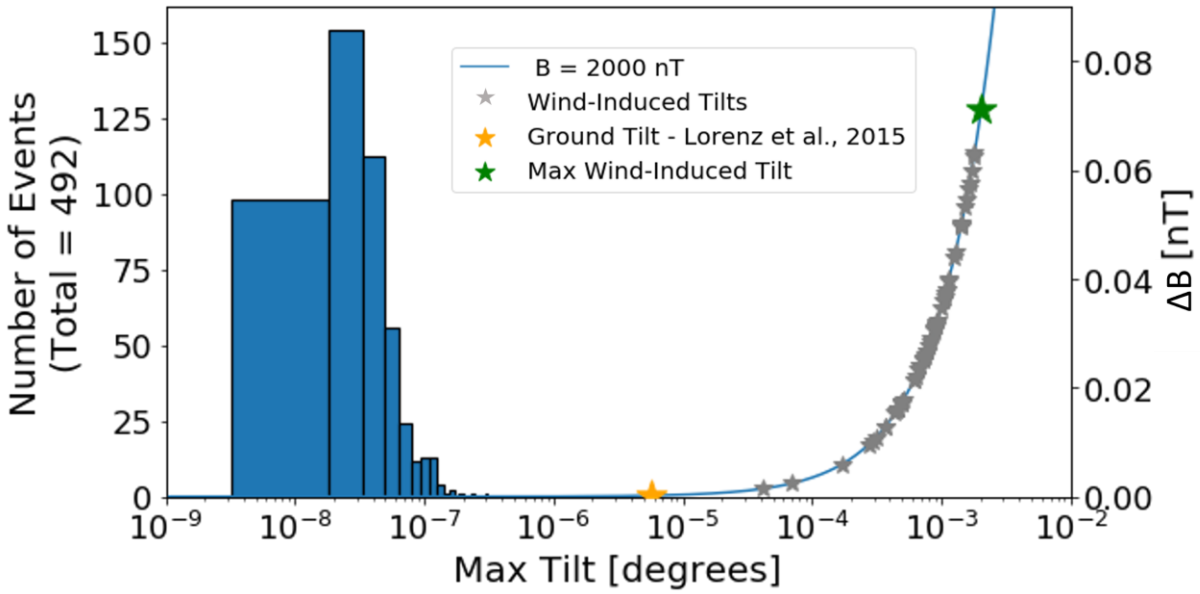


Figure 8*. Expected change in the measured magnetic field strength (ΔB) due to ground tilting of the lander (rotation around a horizontal direction, Section 3.2.1) and wind-induced lander tilt (Section 3.2.2). The reported terrestrial ground tilt (order of magnitude) from Lorenz et al. (2015) with the associated predicted ΔB is shown (orange star), as are the 66 predicted wind-induced tilts at the time of high-SNR$_\sigma$ pressure drops (gray) with the maximum (25.0 m/s wind speed; see section 3.2.2) highlighted in green. Histogram shows ground tilts measured by InSight's seismometer (Murdoch et al., 2021).*

3.2.2 Wind-Induced Lander Tilt

Another possibility is that the lander itself is slightly tilted due to wind loads. Considering, for purposes of exposition, only the drag force on the side of the lander, the moment of this force must be reacted against by the forces on the feet. The feet on the downwind side of the lander place a stronger load on the surface than on the upwind side, and if the ground deforms elastically to provide these different forces, the lander tilts slightly away from the wind. These elastic loads on the ground caused by lander drag and lift are a significant source of noise for the seismometer (e.g. Murdoch et al., 2017), even on the ground a meter or two from the lander. For a deck-mounted instrument, such as the magnetometer, (and in the first days of the landed mission the seismometer), the compliance of the deck to lander wind loads in part results from elastic elements in the landing gear. The transfer function of wind speed to deck movement was estimated by Panning et al. (2020) to be 2.1×10^{-7} $(m/s^2)/(m/s)^2$. We can crudely estimate the lander tilt as being this quantity divided by local gravity 3.7 (m/s^2) – in practice the lander tilt will depend on the wind direction with respect to the lander feet. For our 66 resolvable events, the maximum windspeeds during the pressure drops range from 3.6 to 25.0 m/s. Thus, for a

maximum gust of 26.5 m/s associated with a dust devil, the tilt is ~$25.0^2 \times 2.1 \times 10^{-7} / 3.7 = 3.6 \times 10^{-5}$ radians or 0.002°. Per the foregoing discussion and computations of ΔB from tilts, such a lander tilt can cause an apparent field change of 0.07 nT (Figure 8), and windspeeds would have to reach ~95 m/s to cause the observed signals of ΔB ~ 1 nT. Therefore, while wind-induced lander tilt can affect IFG measurements, to date, windspeeds are not sufficiently large to be the only source of the observed magnetic signals.

3.3 Triboelectric Effects

A magnetic signal could also be generated by swirling charged dust grains entrained in the DD. These grains may become electrically charged via triboelectric effects (contact electrification) in which collisions will charge the particles, and a characteristic charge-to-mass ratio develops (Farrell et al., 2004). This electrification, coupled with the differential movement of particles based on their mass, leads to a magnetic dipole moment and an electric field with an associated magnetic field emission (see Figure 1 in Jackson & Farrell, 2006). The spiraling motion of these charged grains in cyclostrophic balance (in which the inward pressure gradient force balances the outward centripetal force) can be modeled as current loops or a solenoid (Houser et al., 2003; Lorenz, 2016). In this approximation, a DD with fixed parameters would produce a stable magnetic field (see Figure 4 in Houser, Farrell, & Metzger, 2003). However, DDs have constantly fluctuating cross-sectional areas, velocities, and inhomogeneous densities which would result in dynamic magnetic fields (Farrell et al., 2004; Farrell et al., 2006; Lorenz, 2016). Variations on this model have been invoked to explain the two terrestrial measurements of DD magnetic signals (Farrell et al., 2004; Kurgansky et al., 2007), the largest of which was ~0.1 nT (Farrell et al., 2004). Using this approximation, a large dust devil passing with a high density of charged dust grains could be observed by InSight as a quasi-steady magnetic field mostly in the vertical direction (B_z in the lander level frame), possibly with a horizontal field component generated by azimuthal asymmetries, such as multiple vortex cores (Lorenz, 2016).

Recall that no DDs have been detected by InSight's cameras, and only a handful of faint shadows on the solar panels have been detected (Lorenz et al., 2020). Furthermore, Jackson et al. (2021) reported a maximum optical depth of $\tau \sim 0.01$ from InSight's cameras at the times of the dustless vortices. Therefore, a dust-filled vortex would exceed this value of τ. We explore whether an as-yet unobserved vortex containing lofted dust could produce signals in the magnetic field. We consider the case of a 10 m diameter vortex with a dusty annulus, such that the dust content is equivalent to a layer of dust around the perimeter of the vortex that is one particle thick. Thus, the effective area of dust is equal to the circumference of the DD multiplied by the diameter of the dust grains. Assuming a diameter of 2 μm for dust grains, with a grain density 2700 kg/m^3, the mass density per meter height, ρ_M, is ~0.17 kg/m. In reality, the dust is spread over a larger cross-sectional area, for an annulus of width 1 m in a 10 m diameter vortex, this would correspond to a number density of dust grains of ~3×10^{-12} m^{-3}. We further assume that dust has a charge-to-mass ratio, Q/m, of 10^{-6} C/kg (Mendez Harper et al. 2017), the devil rotates once per second (corresponding to a wall circumferential speed, v_w, of 10π m/s, typical of intense vortices (Balme & Greeley, 2006) and at the upper limit as reported for InSight's vortex catalog by Lorenz et al. (2021)). This corresponds to $\rho_M * Q/m * v_w \sim 5.3$ μA of current loop per meter height. The solenoidal vertical magnetic field B inside the devil is then $B = \mu_o * \rho_M * Q/m * v_w = 6.7 \times 10^{-3}$ nT, where $\mu_o = 4\pi 10^{-7}$ Tm/A is the magnetic permeability of free space.

To consider this calculation in the context of our most plausible candidate magnetic signals (Section 2.3), we examined the 4.0 Pa convective vortex on Sol 534 (Figure 4A) to obtain estimates for the event's diameter, trajectory, and miss-distance. We applied the method of Murdoch et al. (2021) that uses the simultaneous pressure and seismic measurements of convective to place constraints on vortex properties and allow reconstruction of their trajectories. The wind speed data (Supplementary Figure 2) shows an increase but no drop at the point of closest approach which would be expected if the eye of the vortex passed directly over the InSight lander. Furthermore, the absence of a sharp change in wind direction supports the inference that InSight is not inside the vortex. The pressure data were fit using the model described in Ellehoj et al. (2010), yielding a slightly different FWHM (11.9s) from the gaussian fit (14.4s FWHM) described in section 2.2. Assuming that the advection speed is the mean background wind speed of 1.9 m/s, the vortex diameter is ~23 m (background wind speed*pressure drop FWHM) (Murdoch et al., 2021). Using seismic data (Supplementary Figure 2), the trajectory of the vortex is found to be in the NE direction during the full encounter, with a closest approach at a distance of ~11.5 m (Figure 9). The seismic and pressure signals from the predicted trajectory were then modeled and compared with the data (Supplementary Figure 3). Given the close proximity of the event(s), the direct ground motion has also been included when generating the synthetic data (see Murdoch et al., 2017 for details). The results show good agreement (Supplementary Figure 3), supporting our trajectory estimate. We note that the proximity of the vortex (the vortex wall just grazing the lander) puts it at the limit of the modeling approach which assumes a far field point source. We attempted a similar analysis for the event on sol 652; however, the simple point source model did not fit the seismic observations well, likely due to the close approach of the vortex.

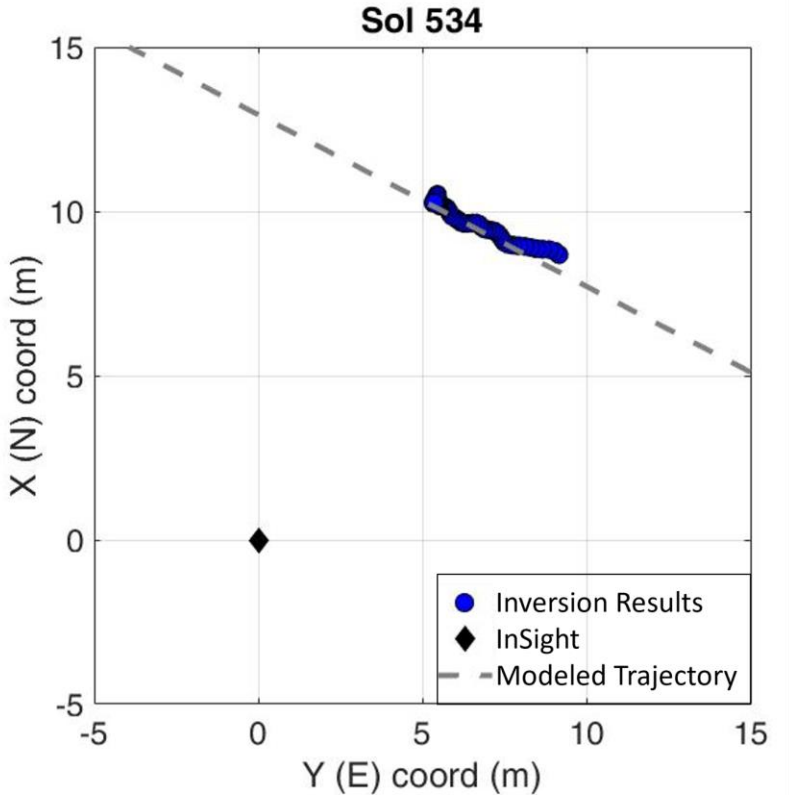


Figure 9. *Trajectory of the 4.0 Pa convective vortex on Sol 534 (Figure 4A). The grey dashed line modeled trajectory is the straight line fit to the pressure and seismic data inversion results in blue.*

We substitute the derived diameter of this close approach event into the triboelectric model calculation above and the resulting DD could generate a magnetic field of ~0.016 nT. Therefore, for this candidate event, the magnetic signal is still an order of magnitude too small to generate the observed signal of ~0.3 nT.

The following question arises: Can triboelectric effects cause a resolvable signature? To answer this question, we explore the extent to which the parameters above - the DD diameter, wall circumferential speed, v_w, dust grain diameter, and the charge-to-mass ratio, *Q/m* - could reasonably be varied. The predicted magnetic field scales linearly with each of these parameters and an order of magnitude increase in total could explain the observed signal amplitudes. Jackson et al. (2021) used models of the pressure and wind speed profiles for their catalog of InSight's vortices to infer intrinsic vortex parameters for a subset of events during which the inferred closest approach distance was within a vortex diameter from the lander. While their most extreme value for DD eyewall velocity of ~37 m/s is similar to our v_w, they report diameters reaching hundreds of meters (a maximum of ~517 m). Clearly this is not the case for the event on sol 534, for which we can estimate the vortex diameter, but other vortices could be larger. Furthermore, our estimate for dust grain diameter (2 μm) is in line with observations for fine atmospheric dust on Mars (Pollack et al., 1995); however, spectral observations during the 2018 dust storm by the Curiosity rover showed dust enhancement by particles ~3 times the typical size (~8 μm) (Lemmon et al. 2019). Terrestrial measurements of dust devil mean grain diameter values range from ~90-100 μm decreasing with height (Raack et al. 2018), although the thin Martian atmosphere may poorly suspend larger grains comparatively (Merrison et al. 2004). Dust grain diameters lifted by a large DD, especially closer to the ground, could therefore be ~5 times larger than we assume. For a constant optical depth, a dust devil comprised of larger grains could allow for a larger signal as their area increases by the square of the grain radius while their mass (and therefore charge density) increases by the grain radius cubed. Alternatively, if large grains are not lifted far from the ground, a shallow toroid of swirling sand rather than a canonical DD may yield the observed magnetic field signature signals. Terrestrial measurements for *Q/m* of sand and volcanic ash can reach maximum values of 10^{-5} C/kg (Tian-Li et al., 2014), while experiments of the Mars dust simulant JSC Mars-1 tribocharged against stainless steel and Teflon have generated *Q/m* ratios much larger (Sharma et al. 2008). The dust concentration could also be higher. In conclusion, higher values for dust devil diameter, dust grain diameter, or *Q*/*m* are plausible and could lead to triboelectrically-driven magnetic fields on the order of 0.1 nT (Section 2.3), for a close DD trajectory.

3.4 Synthesis

We examined several mechanisms that could lead to magnetic signatures during pressure drops. Our investigation of solar array current drops at times of resolvable magnetic signatures shows that SAC changes are present both with and without magnetic signals (and vice versa) and are therefore not the sole contributor to IFG signals. Furthermore, tilt of either the lander or the ground resulting in re-orientation of the IFG with respect to the background crustal field can be

ruled out because the expected and measured tilts reported at InSight are too small to create magnetic signals of resolvable magnitude. Finally, although triboelectric effects are theoretically possible, the estimates made in Section 3.3 indicate that these are not likely to frequently create measurable magnetic fields unless the DD has a large diameter, a very close approach distance and carries sufficient charged dust. A purely solenoidal (i.e. rotationally-symmetric) field from a vertical dust devil would be a quasi-DC signal – increasing slowly from zero as the devil approached, reaching a maximum and then declining. Therefore, if the slow approach and signal generation of a magnetic field-generating vortex was considerably longer than the duration of our pressure drop, our resolvable event detection methodology may not positively detect it.

Convective vortices can also be detected by a corresponding rise in temperature with a core temperature rise of up to 10 K, although elevated temperatures are observed if the sensor enters the vortex core (Ringrose et al. 2007). Because IFG measurements are sensitive to temperature fluctuations (Mittelholz et al. 2020, Thorne et al. 2020), IFG sensor temperature data for all events in Figure 4 were investigated, and we found no corresponding temperature signals. In the case of the event on sol 534 for which we have a derived trajectory, this is consistent with a dust devil that passed close to but not directly over the lander. Furthermore, as shown in Joy et al. (2019), if temperature were the cause, then we should see similar relative changes in the 3 components from one event to another, whose amplitude just depended on the amplitude of the thermal perturbation. This is not the case as can be seen from Figures 4 and 7, e.g. in Figures 4A and 4B, even the signs of the perturbations to B_X and B_Y are opposite. We thus rule out that unmodeled temperature perturbations are responsible for the IFG signals

Although InSight has recorded a large number of pressure drops, there are relatively few with resolvable magnetic signatures. Only 7.7% of pressure drops larger than 1 Pa correlate in time with such magnetic signatures, which is only 0.6% of all recorded pressure drops. Furthermore, given the frequency of pressure drops, it is remarkable that no characteristic DD has been successfully imaged by the ongoing imagery surveys. While DD tracks have been observed around the lander (Perrin et al., 2021), there have been no images of lofted columnar dust at the InSight landing site to date. This is in stark contrast to other martian missions (Lorenz, Spiga, et al., 2021). The dearth of imaged DDs and low proportion of observed magnetic signatures despite numerous measured pressure drops is consistent with a small proportion of convective vortices carrying lofted dust. In most cases with minimal entrained dust solar array currents are largely unaffected with little to no contribution to IFG signals, and triboelectric charging likely does not occur or is minimal.

The local environment at InSight may be a contributing factor to the lack of dust lifting necessary for DD development. While aeolian activity has been reported at InSight including surface creep of particulate and dust removal (Charalambous et al., 2021; Baker et al. 2021), and dust deposition occurs, including critically upon the solar panels (Lorenz, Lemmon, & Maki, 2021), the requirements for saltation leading to DDs may be rarely met. Lorenz, Lemmon, & Maki (2021) estimate that the dust lifting pressure drop threshold at InSight is roughly between 4 and 10 Pa, though they also acknowledge much higher dust lifting thresholds from other Mars missions (6-40 Pa based on data from Pathfinder, Phoenix, and Spirit) and terrestrial observations (20-80 Pa). Furthermore, based on the non-detection of DD's by the InSight camera, Jackson et al. (2021) calculated a localized dust lifting threshold of ~7 Pa. As shown in

Figure 1, such a threshold would exclude most of the pressure drop events examined in this study, even if the observed pressure drop is a lower limit for the actual central pressure drop. By comparing vortex encounters parameters with advective wind speeds Jackson et al. (2021) found evidence that high wind speeds at InSight may have led to the suppression of dust lifting for the most vigorous vortices.

4 Conclusions

We analyzed the magnetic field at InSight at times of pressure drops during the first year of observations to identify if pressure drops might correlate with a magnetic response. We found coincident magnetic field signals, albeit rarely, as 7.7% of data during drops greater than 1 Pa had a magnetic signal in any component. The mechanism that causes these signals is as yet inconclusive, but is not indicative of ground or lander tilting in response to the localized pressure drop (Murdoch et al., 2021). While dust laden convective vortices in close approach could explain our resolvable events, especially those discussed in Section 2.3, our analysis indicates that in general the magnetic signals expected from DDs are too small to be detected. In summary, our observations show (a) no observed magnetic field signal for the vast majority of pressure drops and (b) a few pressure drops, (~9, i.e. < 1% of the overall population of pressure drops > 1Pa) with magnetic field signals < ~1nT, possibly corresponding to more dust laden vortices that would have had to have passed close to the lander. Modeling of pressure and seismic data for one of these 9 pressure drops on sol 534, suggests a vortex diameter of ~23m, and indicates that nominal parameters for dust grain diameter, charge-to mass density, and a dust content corresponding to ~$3x10^{-12}$ particles per m^3, underpredicts the observed magnetic field signal by an order of magnitude. The magnetic field signal depends linearly on all these parameters, as well as on the dust-devil diameter and thus if triboelectric effects are indeed the cause of the full signal during these few pressure drop events, larger values for one or more of the dust parameters are required. The remaining population of events that appear to have an enhanced magnetic signal (high SNR events, ~5% of the pressure drops > 1 Pa) compared with the time intervals immediately preceding and after the pressure drop, are more difficult to assess: some of these comprise very small signals (< ~0.1 nT) that could potentially be consistent with DD related signatures, however larger signals, especially those > 1 nT would require DD parameters outside the limit of current studies

A larger number of events with 2 Hz IFG data and 0.2 Hz solar array current data could strengthen this investigation, as would an unambiguous event detection by InSight's cameras to provide a positive control. Analysis of the coincidence of solar array current signals and IFG signals is limited by the intermittent nature of the SAC data. However, the DD solar panel cleaning events which were anticipated have not yet transpired and the power constraints during the current winter season resulting from the accumulation of dust on the solar panels have led to IFG not collecting continuous data since late 2020. Further martian missions with meteorological instruments and magnetometers, such as China's Tianwen Zhurong lander, could also address the magnetic signals associated with pressure drops and DDs (Du et al., 2020), as could continued terrestrial studies like those of the MATADOR campaign in the Arizona desert (Renno et al., 2004; Farrell et al., 2004). Further understanding of DDs can help explain why they have not yet been imaged at the InSight landing site, while all other Mars surface missions with visual cameras have imaged several cases of dust devils (Ferri et al., 2003, Ellehoj et al., 2010).

Acknowledgments

We acknowledge NASA, CNES, their partner agencies and Institutions (UKSA, SSO, DLR, JPL, IPGP-CNRS, ETHZ, IC, MPS-MPG) and flight operations team at JPL, SIS-MOC (SEIS on Mars Operations Center) and MSDS (Mars SEIS Data Service). We acknowledge support from the Natural Sciences and Engineering Research Council of Canada (S.T, C.L.J.), the Canadian Space Agency and the InSight Mission (C.L.J.), CNES in the frame of the InSight mission (A.S, B.L.), as well as ETH 19-2 FEL-34 and funding through the Harvard Daly Fellowship (A.M.). All InSight data used in this study are publicly available in the Planetary Data System: InSight IFG calibrated data https://doi.org/10.17189/1519202 and Calibration data https://doi.org/10.17189/1510486. This paper is InSight Contribution Number, ICN 231.

References

Atreya, S. K., Wong, A. S., Renno, N. O., Farrell, W. M., Delory, G. T., Sentman, D. D., … Catling, D. C. (2006). Oxidant enhancement in Martian dust devils and storms: Implications for life and habitability. *Astrobiology*, *6*(3), 439–450. https://doi.org/10.1089/ast.2006.6.439

Baker, M., Newman, C., Charalambous, C., Golombek, M., Spiga, A., Banfield, D., et al. (2021). Vortex-dominated aeolian activity at InSight's landing site, Part 2: Local meteorology, transport dynamics, and model analysis. *Journal of Geophysical Research: Planets, 126*, e2020JE006514. https://doi.org/10.1029/2020JE006514

Balme, M., & Greeley, R. (2006). Dust devils on Earth and Mars. *Reviews of Geophysics*, *44*(3), RG3003. https://doi.org/10.1029/2005RG000188

Banerdt, W. B., Smrekar, S. E., Banfield, D., Giardini, D., Golombek, M., Johnson, C. L., … Wieczorek, M. (2020). Initial results from the InSight mission on Mars. *Nature Geoscience*. https://doi.org/10.1038/s41561-020-0544-y

Bo, T. L., Zhang, H., & Zheng, X. J. (2014). Charge-to-mass ratio of saltating particles in wind-blown sand. *Scientific Reports*, *4*. https://doi.org/10.1038/srep05590

Banfield, D, Rodriguez-Manfredi, J. A., Russell, C. T., Rowe, K. M., Leneman, D., Lai, H. R., … Team, T. T. (2018). InSight Auxiliary Payload Sensor Suite (APSS). *Space Science Reviews*, *215*(1), 4. https://doi.org/10.1007/s11214-018-0570-x

Banfield, D., Spiga, A., Newman, C., Forget, F., Lemmon, M., Lorenz, R., … Banerdt, W. B. (2020). The atmosphere of Mars as observed by InSight. *Nature Geoscience*, *13*(3), 190–198. https://doi.org/10.1038/s41561-020-0534-0

Charalambous, C., McClean J., B., Baker, M., Pike, W. T., Golombek, M., Lemmon, M., … Banerdt, W. B. (2021). Vortex-dominated aeolian activity at InSight’s landing site, Part 1: Multi-instrument Observations, Analysis and Implications. *Journal of Geophysical Research: Planets*. https://doi.org/10.1029/2020je006757

Chatain, A. and Spiga, A. and the InSight team: Seasonal variability of Mars atmospheric turbulence studied from InSight high-frequency pressure measurements, E*uropean Planetary Science Congress 2021*, online, 13–24 Sep 2021, EPSC2021-290, https://doi.org/10.5194/epsc2021-290, 2021.

Du, A. M., Zhang, Y., Li, H. Y., Qiao, D. H., Yi, Z., Zhang, T. L., … Dai, J. L. (2020). The Chinese Mars ROVER Fluxgate Magnetometers. *Space Science Reviews*. https://doi.org/10.1007/s11214-020-00766-8

Ellehoj M. D., Gunnlaugsson H. P., Taylor P. A. et al. (2010). Convective vortices and dust devils at the Phoenix Mars mission landing site. *Journal of Geophysical Research*. https://doi.org/10.1029/2009JE003413

Farrell, W. M., Smith, P. H., Delory, G. T., Hillard, G. B., Marshall, J. R., Catling, D., … Johnson, B. (2004). Electric and magnetic signatures of dust devils from the 2000-2001 MATADOR desert tests. *Journal of Geophysical Research E: Planets*, *109*(3). https://doi.org/10.1029/2003je002088

Farrell, William M., Marshall, J. R., Cummer, S. A., Delory, G. T., & Desch, M. D. (2006). A model of the ULF magnetic and electric field generated from a dust devil. *Journal of Geophysical Research E: Planets*, *111*(11), E11004. https://doi.org/10.1029/2006JE002689

Fenton, L. K., & Lorenz, R. (2015). Dust devil height and spacing with relation to the Martian planetary boundary layer thickness. *Icarus*. https://doi.org/10.1016/j.icarus.2015.07.028

Ferri F., Smith P. H., Lemmon, M., Renno, N. O. (2003) Dust devils as observed by Mars Pathfinder. *Journal of Geophysical Research*. https://doi.org/10.1029/2000JE001421

Harrison, R. G., Barth, E., Esposito, F., Merrison, J., Montmessin, F., Aplin, K. L., … Zimmerman, M. (2016). Applications of Electrified Dust and Dust Devil Electrodynamics to Martian Atmospheric Electricity. *Space Science Reviews*, Vol. 203, pp. 299–345. https://doi.org/10.1007/s11214-016-0241-8

Houser, J. G., Farrell, W. M., & Metzger, S. M. (2003). ULF and ELF magnetic activity from a terrestrial dust devil. *Geophysical Research Letters*, *30*(1). https://doi.org/10.1029/2001GL014144

Jackson, T. L., & Farrell, W. M. (2006). Electrostatic fields in dust devils: An analog to Mars. *IEEE Transactions on Geoscience and Remote Sensing*, *44*(10), 2942–2949. https://doi.org/10.1109/TGRS.2006.875785

Jackson, B., Crevier, J., Szurgot, M., Battin, R., Clement, P., Rodriguez, S. (2021) Inferring Vortex and Dust Devil Statistics from InSight. *The Planetary Science Jorunal, 2 206.* https://doi.org/10.3847/PSJ/ac260d

Johnson, C. L., Mittelholz, A., Langlais, B., Russell, C. T., Ansan, V., Banfield, D., … Banerdt,

W. B. (2020). Crustal and time-varying magnetic fields at the InSight landing site on Mars. *Nature Geoscience*, *13*(3), 199–204. https://doi.org/10.1038/s41561-020-0537-x

Joy, S. P., Mafi, J. N., & Slavney, S. (2019). Interior Exploration Using Seismic Investigations, Geodesy, and Heat Transport (InSight) Mission Insight Fluxgate Magnetometer (IFG) PDS Archive Software Interface Specification. *urn:nasa:pds:insight-ifg-mars:document:insight-ifg-sis*.

Kahre, M. A., Murphy, J. R., & Haberle, R. M. (2006). Modelling the Martian dust cycle and surface dust reservoirs with the NASA Ames general circulation model. *Journal of Geophysical Research E: Planets*. https://doi.org/10.1029/2005JE002588

Kok, J. F., and Renno, N. O. (2009), Electrification of wind-blown sand on Mars and its implications for atmospheric chemistry, *Geophys. Res. Lett.*, 36, L05202, doi:10.1029/2008GL036691.

Kurgansky, M. V, Baez, L., & Ovalle, E. M. (2007). A simple model of the magnetic emission from a dust devil. *Journal of Geophysical Research E: Planets*, *112*(11), 11008. https://doi.org/10.1029/2007JE002952

Lemmon, M. T., Guzewich, S. D., McConnochie, T., de Vicente-Retortillo, A., Martínez, G., Smith, M. D., … Jacob, S. (2019). Large Dust Aerosol Sizes Seen During the 2018 Martian Global Dust Event by the Curiosity Rover. *Geophysical Research Letters*, *46*(16). https://doi.org/10.1029/2019GL084407

Lognonné, P., Banerdt, W. B., Pike, W. T., Giardini, D., Christensen, U., Garcia, R. F., … Zweifel, P. (2020). Constraints on the shallow elastic and anelastic structure of Mars from InSight seismic data. *Nature Geoscience*. https://doi.org/10.1038/s41561-020-0536-y

Lorenz, R. D. (2016). Heuristic estimation of dust devil vortex parameters and trajectories from single-station meteorological observations: Application to InSight at Mars. *Icarus*, *271*, 326–337. https://doi.org/10.1016/j.icarus.2016.02.001

Lorenz, R. D., & Jackson, B. K. (2015). Dust devils and dustless vortices on a desert playa observed with surface pressure and solar flux logging. *GeoResJ*. https://doi.org/10.1016/j.grj.2014.11.002

Lorenz, R. D., Kedar, S., Murdoch, N., Lognonné, P., Kawamura, T., Mimoun, D., & Banerdt, W. B. (2015). Seismometer detection of dust devil vortices by ground tilt. *Bulletin of the Seismological Society of America*, *105*(6), 3015–3023. https://doi.org/10.1785/0120150133

Lorenz, R. D., Lemmon, M. T., & Maki, J. (2021). First mars year of observations with the InSight solar arrays: Winds, dust devil shadows, and dust accumulation. *Icarus*. https://doi.org/10.1016/j.icarus.2021.114468

Lorenz, R. D., Lemmon, M. T., Maki, J., Banfield, D., Spiga, A., Charalambous, C., … Banerdt, W. B. (2020). Scientific Observations With the InSight Solar Arrays: Dust, Clouds, and Eclipses on Mars. *Earth and Space Science*. https://doi.org/10.1029/2019EA000992

Lorenz, R. D., & Reiss, D. (2015). Solar panel clearing events, dust devil tracks, and in-situ vortex detections on Mars. *Icarus, 248,* 162–164. https://doi.org/10.1016/J.ICARUS.2014.10.034

Lorenz, R. D., Spiga, A., Lognonné, P., Plasman, M., Newman, C. E., & Charalambous, C. (2021). The whirlwinds of Elysium: A catalog and meteorological characteristics of "dust devil" vortices observed by InSight on Mars. *Icarus, 355,* 114119. https://doi.org/10.1016/j.icarus.2020.114119

Méndez Harper, J., McDonald, G., Dufek, J. Malaska, M. J., Burr D. M., Hayes, A. G., McAdams, J., Wray, J. J. (2017). Electrification of sand on Titan and its influence on sediment transport. *Nature Geoscience 10, 260–265* https://doi.org/10.1038/ngeo2921

Merrison, J. P., Bertelsen, P., Frandsen, C., Gunnlaugsson, P., Knudsen, J. M., Lunt, S., … Uggerhøj, E. (2002). Simulation of the Martian dust aerosol at low wind speeds. *Journal of Geophysical Research E: Planets, 107*(12). https://doi.org/10.1029/2001je001807

Mittelholz, A., Johnson, C. L., Thorne, S. N., Joy, S., Barrett, E., Fillingim, M. O., … Banerdt, W. B. (2020). The Origin of Observed Magnetic Variability for a Sol on Mars From InSight. *Journal of Geophysical Research: Planets, 125*(9). https://doi.org/10.1029/2020JE006505

Mittelholz, A., Johnson, C. L., Thorne, S. N., Yau, V., Joy, S., Barrett, E., … Banerdt, W. B. (2021). Magnetic Variations of a Sol Observed Over a Year on Mars with InSight. Lunar and Planetary Science Conference. *LPI Contributions 2548*. https://www.hou.usra.edu/meetings/lpsc2021/pdf/1941.pdf

Murdoch, N., Spiga, A., Lorenz, R., Garcia, R. F., Perrin, C., Widmer-Schnidrig, R., … Banerdt, W. B. (2021). Constraining Martian Regolith and Vortex Parameters From Combined Seismic and Meteorological Measurements. *Journal of Geophysical Research: Planets*. https://doi.org/10.1029/2020JE006410

Murdoch, N., Mimoun, D., Garcia, R. F., Rapin, W., Kawamura, T., Lognonné, P., … Banerdt, W. B. (2017). Evaluating the Wind-Induced Mechanical Noise on the InSight Seismometers. *Space Science Reviews*. https://doi.org/10.1007/s11214-016-0311-y

Panning, M. P., Pike, W. T., Lognonné, P., Banerdt, W. B., Murdoch, N., Banfield, D., … Warren, T. (2020). On-Deck Seismology: Lessons from InSight for Future Planetary Seismology. *Journal of Geophysical Research: Planets*. https://doi.org/10.1029/2019JE006353

Pollack, J. B., Ockert-Bell, M. E., & Shepard, M. K. (1995). Viking Lander image analysis of Martian atmospheric dust. *Journal of Geophysical Research*, *100*(E3). https://doi.org/10.1029/94JE02640

Raack, J., Reiss, D., Balme, M. R., Taj-Eddine, K., & Ori, G. G. (2018). In Situ Sampling of Relative Dust Devil Particle Loads and Their Vertical Grain Size Distributions. *Astrobiology*, *18*(10). https://doi.org/10.1089/ast.2016.1544

Renno, N. O., Abreu, V. J., Koch, J., Smith, P. H., Hartogensis, O. K., De Bruin, H. A., Burose, D., Delory, G. T., Farrell, W. M., Watts, C. J., & Garatuza, J. (2004). MATADOR 2002: A pilot field experiment on convective plumes and dust devils. *Journal of Geophysical Research: Planets*, 109(E7), E07001. https://doi.org/10.1029/2003JE002219

Ringrose, T. J., Patel, M. R., Towner, M. C., Balme, M., Metzger, S. M., & Zarnecki, J. C. (2007). The meteorological signatures of dust devils on Mars. *Planetary and Space Science*, *55*(14). https://doi.org/10.1016/j.pss.2007.07.002

Sharma, R., Clark, D. W., Srirama, P. K., & Mazumder, M. K. (2008). Tribocharging characteristics of the Mars dust simulant (JSC Mars-1). *IEEE Transactions on Industry Applications*, *44*(1). https://doi.org/10.1109/TIA.2007.912761

Spiga, A., Barth, E., Gu, Z., Hoffmann, F., Ito, J., Jemmett-Smith, B., … Wei, W. (2016). Large-Eddy Simulations of Dust Devils and Convective Vortices. *Space Science Reviews*. https://doi.org/10.1007/s11214-016-0284-x

Spiga, A., Murdoch, N., Lorenz, R., Forget, F., Newman, C., Rodriguez, S., … Banerdt, W. B. (2021). A study of daytime convective vortices and turbulence in the Martian planetary boundary layer based on half-a-year of InSight atmospheric measurements and large-eddy simulations. *Journal of Geophysical Research: Planets*, 126, e2020JE006511. https://doi.org/10.1029/2020JE006511

Stähler, S. C., Widmer-Schnidrig, R., Scholz, J.-R., van Driel, M., Mittelholz, A., Hurst, K., … et al. (2020). Geophysical observations of Phobos transits by InSight. *Earth and Space Science Open Archive*, 15. https://doi.org/10.1002/essoar.10503257.1

Stott, A. E., Garcia, R. F., Pinot, B., Murdoch, N., Mimoun, D., Spiga, A., Banfield, D., Navarro, S., Mora-Sotomayor, L., Charalambous, C., Pike, W. T., Lognonné, P., and Horleston, A.: Atmospherically driven ground motion at InSight: a machine learning perspective, *EGU General Assembly 2021*, online, 19–30 Apr 2021, EGU21-12344, https://doi.org/10.5194/egusphere-egu21-12344, 2021

Thomas, P., & Gierasch, P. J. (1985). Dust devils on Mars. *Science*. https://doi.org/10.1126/science.230.4722.175

Thorne, S. N., Mittelholz, A., Johnson, C. L., Joy, S., Liu, X., Russell, C. T., … Banerdt, W. B. (2020). InSight fluxgate magnetometer data calibration assessment and implications. *LPI Contributions 2089*.